JOURNAL OF PROPULSION AND POWER
Vol. 21, No. 4, July–August 2005

Visualization of Flow Development in Hybrid Rocket Motors with High Regression Rates

Venelin Stamatov,* Damon R. Honnery,† and Julio Soria‡
Monash University, Clayton, Victoria 3800, Australia

The effect of fuel surface regression on the structure of the flow in a hybrid rocket motor is examined at isothermal conditions using an expanding backward-facing step flow in a wind tunnel. It is shown that the long time oxidizer flow structure is almost independent of the simulated fuel regression rate. During the regression phase and for cases of high ratio of the oxidizer freestream velocity to the simulated fuel regression rate, the oxidizer flow evolves in a quasi-stationary manner, where the instantaneous backward-facing step flow structure is akin to that of the static case.

Nomenclature

H	=	h_t/h
h	=	final step height, m
h_t	=	displacement of the floor at time t, m
Re_h	=	Uh/ν
t	=	time, s
t_f	=	time for the full displacement of the floor, s
U	=	freestream velocity, m/s
U_r	=	U/u
u	=	maximal velocity of the floor, m/s
u_t	=	velocity of the floor at time t, m/s
x, y	=	rectangular Cartesian coordinates, m
Y	=	u_t/u
η	=	maximum in-plane displacement based on U, pixel
ν	=	fluid viscosity, m^2/s
τ	=	t/t_f
χ	=	spatial resolution, m
ω	=	vorticity of the flow, s^{-1}
ω'	=	$\omega h/U$

Introduction

TWO basic types of chemical rocket propulsion systems, liquid and solid, are widely used. In the liquid rocket motor (LRM), liquid fuel and oxidizer are fed at high pressure to a combustion chamber, where they mix and react producing high-temperature, high-pressure gases, which exhaust through a nozzle. In the solid rocket motor (SRM), the solid fuel and oxidizer are intimately mixed and allowed to cure inside the rocket case, producing an explosive propellant in the form of tubes of various shape and lengths known as fuel cells or grains. Usually, a central core that extends the full length of the grain is introduced to increase the propellant surface area initially exposed to combustion. On ignition, the solid fuel burns uninterrupted until all of the fuel is exhausted. The combustion area of a SRM with central, cylindrical port changes as the inner surface burns outward. The solid fuel core shape has a profound influence on the shape of the thrust–time profile of an SRM. For instance, a star or rod and tube grain provides an approximately neutral burn because the surface area remains fairly constant throughout the burn duration, a tubular fuel grain provides a progressive burn, whereas a double anchor shape of the core results in a regressive burn.

In contrast to these two common types of rocket motors is the hybrid rocket motor (HRM), in which the fuel is stored in the solid phase and the oxidizer in the fluid phase. Typically, in the HRM the oxidizer is injected into the combustion chamber, the walls of which form the solid fuel. The injected oxidizer flows axially along the port, forming a boundary layer over the solid fuel. On ignition, a flame sheet is formed above the solid surface. A schematic of an HRM is shown in Fig. 1. Similar to the SRM, in an HRM the combustion area and chamber pressure can be kept more or less constant, or it can follow a certain operational curve, depending on the exact shape of the grain.

The HRM has advantages over the liquid and solid propellant rockets: (1) It is less complex in design than LRMs. (2) It has potentially higher reliability. (3) It has lower fire and explosion hazards. (Hybrid motors are inherently immune to explosion.) (4) It has lower development and operating costs than LRMs and a higher specific impulse than SRMs. (5) Unlike SRMs, it has an ability for thrust termination, restart, and throttling. However, the low-thrust output is a serious disadvantage of HRMs, making them an unattractive option.

For HRMs to become practical, higher rates of fuel mass transfer and, therefore, higher fuel burn rates are required. An approach to increase the rate of fuel mass transfer is to use high regression rate cryogenic HRMs.[1] Another approach to increase the fuel-burning rate is to use solid fuels the surface of which undergoes melting because of the flame radiation. Entrainment of droplets from the liquid–gas interface can substantially increase the rate of fuel mass transfer leading to much higher surface regression rates and thrust output than can be achieved with conventional HRM fuels.[2,3] The general theory of the combustion of liquefying hybrid propellants and a study of the stability of liquid films may be found in Refs. 4 and 5.

Turbulence significantly affects the complex physical and chemical processes in the combustion chamber. Nevertheless, because of the extreme temperature conditions and the aggressiveness of the gas phase, there are currently no reliable experimental methods to study the flow development inside the combustion chamber of HRMs. Chiaverini et al.[6,7] used real-time, x-ray radiography to obtain instantaneous solid-fuel regression rate data. The semi-empirical local regression-rate correlations, combined with computational fluid dynamics (CFD) calculations, could provide some indirect information about the flow development.

In all cases, as fuel regression rates increase, the dynamic nature of the regressing fuel surface relative to the oxidizing flow could become important. For example, the question of whether it is oxidizing fluid momentum that dominates the core flow in this environment needs to be addressed. Stamatov et al.[8–10] proposed a novel, convenient method for study of the internal flow development inside the combustion chamber of a high regression rate HRM. In Refs. 8–10,

Received 30 June 2004; revision received 24 March 2005; accepted for publication 22 February 2005.

*Research Fellow, Laboratory for Turbulence Research in Aerospace and Combustion, Department of Mechanical Engineering.

†Senior Lecture, Laboratory for Turbulence Research in Aerospace and Combustion, Department of Mechanical Engineering.

‡Professor, Laboratory for Turbulence Research in Aerospace and Combustion, Department of Mechanical Engineering.

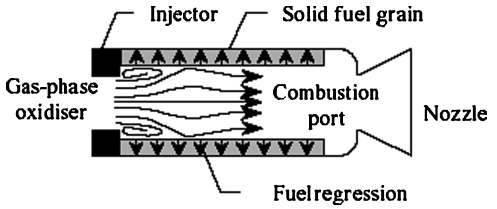

Fig. 1 Schematic of an HRM.

the effect of the fuel surface regression on the structure of the flow in an HRM at isothermal conditions is examined using an expanding backward-facing step (BFS) flow in a wind tunnel. This work is expanded here. Three different expanding BFS modes of the flow are considered. Two nonintrusive laser diagnostic techniques are used. The Mie scattering diagnostic technique is used for instantaneous flow visualization. Multigrid cross-correlation digital particle image velocimetry (MCCDPIV) is used to measure the instantaneous two-components, two-dimensional velocity field. Ensemble-averaged, normalized, in-plane velocity, and out-of-plane vorticity fields downstream of the expanding BFS for several time steps are shown. The dependence of the normalized value of the maximal clockwise vorticity in the recirculation zone core on time is used to measure the oxidizer flow momentum dominance over the entrainment of the flow caused by the fuel regression simulated by the floor. These results are then considered in relation to results from the thrust output measurements that have been conducted in the Laboratory for Turbulence Research in Aerospace and Combustion (LTRAC) Monash University, Australia, on a laboratory-scale, high regression rate HRM by using a liquefying solid fuel.

Experimental Apparatus and Methodology

The experimental investigations are conducted in a channel flow, open-circuit wind tunnel. The tunnel is shown in Fig. 2. The working section of the tunnel is shown in detail in Fig. 3. The flow velocity used to simulate the oxidizer flow is controlled by a motor controller, connected to a 5.5-kW electrical motor and an in-line centrifugal blower. The airflow is seeded by using olive oil droplets, produced by a Laskin-type nozzle seed generator. The generator produces microspheres of about 1 μm diameter. The wind-tunnel horizontal working section is made from perspex and is 0.85 m long, 1.0 m wide, with a height of 0.1 m. The floor of the working section, used to simulate the fuel surface, can move by up to 0.07 m downward, forming a BFS. This movement is used to simulate the regression of the fuel. Because the tunnel is open to the atmosphere, movement of the floor may result in flow reversal at the exit of the test section. A stepper motor and a computer-controlled indexer control the position, velocity, and acceleration of the floor. A photodiode is used to detect the motion of the floor and trigger the image acquisition.

A 10-mW He–Ne laser operating at 632.8 nm is used for the Mie scattering flow visualization. A twin, frequency-doubled Nd:YAG pulsed laser is used to generate 532-nm laser sheets to illuminate the two-dimensional plane of the seeded flow for the particle image velocimetry (PIV) experiments. The laser system is capable of producing a maximum energy per pulse of 200 mJ, with a pulse width of approximately 6 ns and a maximum repetition rate of up to 10 Hz. It was normally operated at 75% of its maximal power. An appropriate combination of cylindrical and spherical lenses inside the articulated laser arm produces a 0.1 m wide by 0.002 m thick collimated light sheet.

The scattered light from the seed particles is imaged using a 12-bit 1280×1024 pixel digital camera. The camera is coupled with a Pentium-based personal computer with image acquisition and data processing software. The images are captured at multiple x–y planes by traversing the camera across the desired regions along the centerline of the wind tunnel. In the case of PIV measurements, the time between two consecutive ensemble-matched image pair acquisitions is set to 5 s to ensure that consecutive velocity fields are statistically independent.

Three different displacement modes of the floor of the working section are considered in this work. In the first mode, the floor

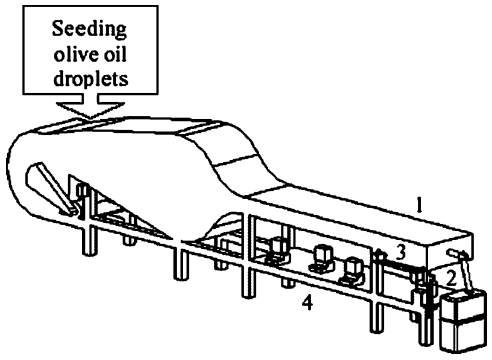

Fig. 2 Channel flow, open-circuit, wind tunnel at LTRAC (not to scale): 1) working section, 2) laser, 3) digital camera, and 4) computers.

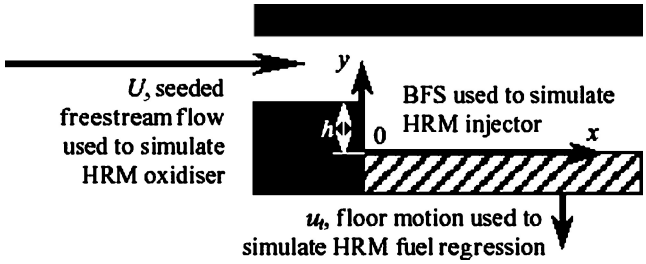

Fig. 3 Working section of the wind tunnel (not to scale).

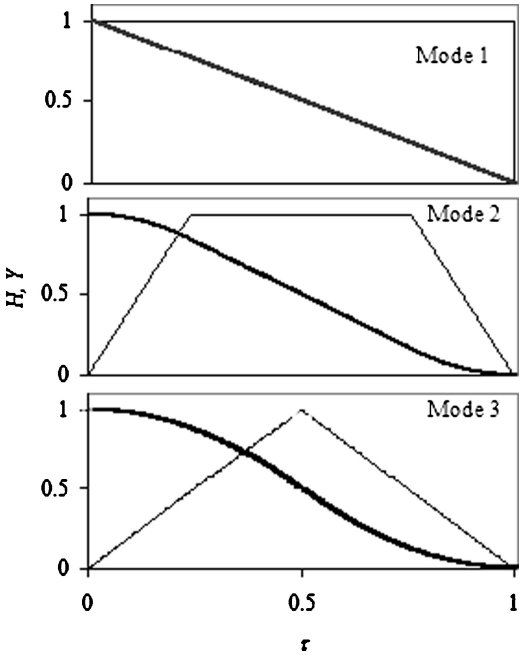

Fig. 4 Normalized displacement and velocity of the floor of the working section of the wind tunnel vs normalized time τ: ——, H and ——, Y.

maximal velocity is set to 0.0005 m/s; in the second mode, it is set to 0.08 m/s; and in the third, it is set to 0.141 m/s. In all cases, the acceleration and deceleration of the plate is fixed to 1 m/s^2. The normalized floor displacement H and velocity Y profiles used are shown in Fig. 4. In terms of simulation of different fuel burning modes, modes 1 and 2 correspond to a typical neutral burn with rapid ignition and extinction time in the first case and a prolonged ignition period for mode 2. The floor motion in mode 3 allows a subsequent simulation of progressive and regressive burn modes.

The Mie scattering experiments are conducted using the first displacement mode (floor maximal velocity of 0.0005 m/s at a freestream velocity of 0.7 m/s and a final step height of 0.005 m). The Reynolds number, Re_h, based on the final step height and freestream velocity, is 239.5. The ratio between the freestream velocity and the maximal velocity of the floor, U_r, is fixed to 1400. Instantaneous

Table 1 Experimental conditions for four different cases for PIV measurements

Parameter	Mode 1, case 1	Mode 2, case 2	Mode 3	
			case 3	case 4
u, m/s	0.0005	0.08	0.141	0.141
U_r	1400	8.75	4.96	7.27
h, m	0.01	0.02	0.02	0.02
χ	$0.08h$	$0.05h$	$0.05h$	$0.05h$
U, m/s	0.7	0.7	0.7	1.025
Re_h	479	959	959	1404
t_f	2 s	330 ms	282 ms	282 ms
η, pixels	57.3	43.5	43.5	63.7

images are taken every 40 ms. A 50-mm Nikon lens provided a field of view $(x, y) = 0.058 \times 0.073$ m.

A MCCDPIV analysis algorithm developed by Soria[11,12] is used to acquire instantaneous, in-plane velocity field and out-of-plane vorticity measurements of the BFS flow. The MCCDPIV image processing technique is chosen because of its advantage over other techniques due to the higher dynamic range and greater measurement accuracy obtained through the use of an adaptive integration window displacement process. The PIV analysis of the images acquired in the x–y planes used a 32×32 pixel final interrogative window. A fractional error of 1.4% (referenced to the freestream velocity) exists in the instantaneous velocity field measurements. Velocity fields not satisfying a criterion of at least 95% successfully computed vectors are discarded. Rejected vectors were not used in the ensemble-averaged mean velocity fields. To provide qualitative information regarding the fluid structure, 10 image pairs per ensemble average are taken.

Far- and near-field PIV experiments are done together with measurements of the flow in the area of the wind tunnel before the BFS, which is the analog of the oxidizer port in an HRM. The far-field PIV images provide a general representation of the flow development for eight consecutive locations of the camera along the centerline of the working section of the wind tunnel, covering a distance x/h from 0 to 15. The measurements correspond to the motion of the floor of the working section of the wind tunnel with a velocity of 0.08 m/s, acceleration of 1 m/s^2 and final displacement of the floor of 0.02 m. The freestream velocity is 0.7 m/s, $U_r = 8.75$, and $Re_h = 959$. Note, these are the experimental conditions that are also used in case 2 of the near-field PIV measurements.

The near-field experiments provide greater details about the zone near the BFS. The measurements are conducted for two locations of the camera, covering a normalized distance along the centerline of 3.8 x/h. Two freestream velocities of 0.7 and 1.025 m/s are used, which results in four ratios of freestream velocity to the velocity of the floor.

The experimental conditions for the four cases of interest for the near-field PIV measurements are summarized in Table 1.

The thickness of the boundary layer just upstream of the moving section is $2.6h$ for case 1, $1.3h$ for cases 2 and 3, and $1.1h$ for case 4.

A 200-mm Micro Nikkor lens is used for imaging case 1, providing a field of view $(x, y) = 0.031 \times 0.025$ m. A 105-mm lens is used for far field, cases 2–4, and the zone before the BFS imaging, providing a field of view $(x, y) = 0.041 \times 0.033$ m.

Results

Mie Scattering Visualization

The temporal evolution of the process of BFS expanding flow is shown in Fig. 5 using instantaneous Mie scattering images for $U_r = 1400$. The seed particles in these images take on the appearance of streaks whose length is indicative of their velocity.

It can be seen that initially ($\tau = 0.2$) the flow follows the motion of the floor. The expansion due to the change of surface geometry imposes an adverse pressure gradient on the flow and causes the boundary layer to separate at the step edge. Immediately after detachment, the flow essentially behaves as a free boundary layer, with high-speed fluid on one side and low-speed fluid on the other.

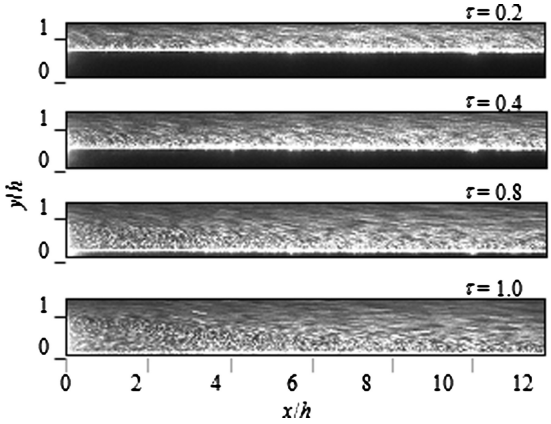

Fig. 5 Instantaneous Mie scattering images of the flow near the expanding BFS for several time steps, $U_r = 1400$ and $Re_h = 239.5$.

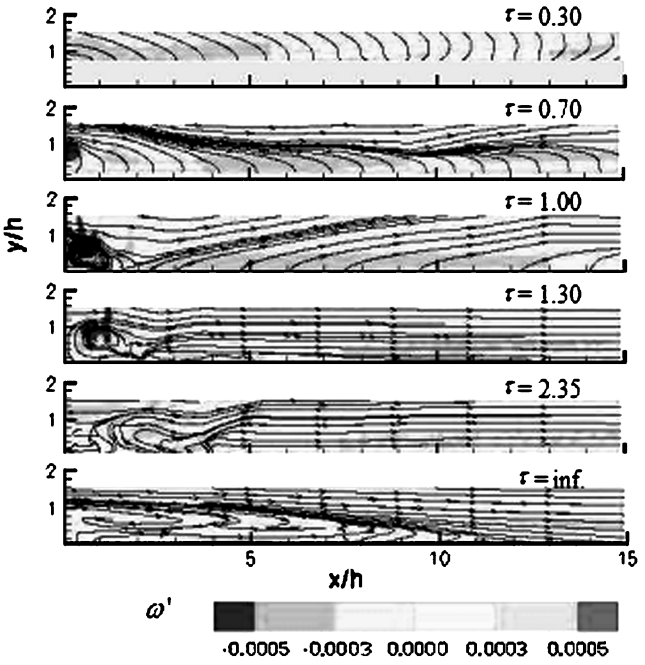

Fig. 6 Far-field, ensemble-averaged, normalized out-of-plane vorticity fields and positions of streamlines downstream expanding BFS, case 2; floor position of working section of wind tunnel in gray.

Some distance downstream, the boundary layer impinges the surface and forms a closed recirculation region containing upstream moving fluid. The region of clockwise recirculating flow clearly appears for the first time at $\tau = 0.4$. The recirculation zone remains attached to the BFS and stretches and enlarges as the plate moves downward ($\tau = 0.4$–1.0).

The boundary-layer reattachment region moves downstream with time; however, it is always at such a distance from the BFS (8–12 x/h_t) that is typical for the static BFS flow.[13] This in turn suggests that at this value of the ratio U_r the flow responds faster than the movement of the floor, and the flow shows the main features of a static BFS flow.

PIV Far-Field Measurements

The ensemble-averaged, normalized out-of-plane vorticity fields and positions of the streamlines downstream expanding BFS for several time steps are presented in Fig. 6 for case 2. The normalized out-of-plane vorticity field and positions of the streamlines of BFS flow in which the step height is fixed ($\tau =$ infinity) is also shown in Fig. 6 for comparison.

Note that the flow structure is dynamic with three characteristic phases: evolution ($0 < \tau < 1.0$), transition ($1.0 < \tau < 2.35$), and

relaxation ($\tau > 2.35$). Initially, the flow is dominated by the production of a step-driven vortical structure located near the step corner. Completion of the step movement sees elongation or stretching of the vortical structure by the freestream. The vortical structure and the boundary-layer reattachment point move downstream as time progresses.

PIV Near-Field Measurements

PIV near-field measurements are done at various ratios of freestream velocity to the velocity of the floor. The ensemble-averaged, planar, two-component velocity fields, out-of-plane vorticity of the flow, and the positions of the integrated streamlines of the PIV near-field measurements are shown in Figs. 7–10. The vectors are colored, indicating the normalised vorticity ω', and only every second vector is shown for clarity. The position of the floor of the working section of the wind tunnel is marked in gray in Figs. 7–10.

The ensemble-averaged velocity fields reveal that the motion of the flow is strongly influenced by the ratio of freestream velocity to the velocity of the floor. In case 1, Fig. 7, in which U_r is the highest (Table 1), the flow shows features of a static BFS flow, that is, the flow response is faster than the movement of the floor. There is a stretched downstream clockwise recirculating region, which can be seen even in the earliest image ($\tau_1 = 0.2$). The boundary-layer reattachment region moves downstream with time, constantly remaining on a distance of about 8–12 x/h_t from the BFS, which is typical for the static BFS flow.

The flow behaves differently in the other three cases of lower U_r. In case 2 (Fig. 8), the motion of the floor of the working section of the wind tunnel intensively entrains the flow. As the floor accelerates, so does the attached fluid. The expansion due to the change of surface geometry imposes an adverse pressure gradient on the flow, and a region of clockwise recirculating flow appears and enlarges as the plate moves downward. Initially the center of rotation is attached to

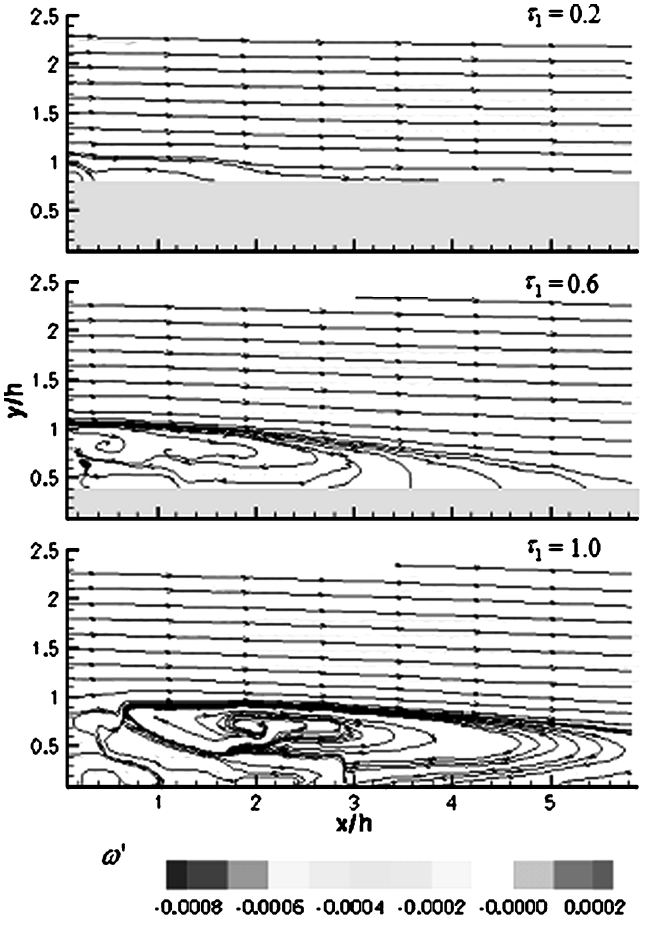

Fig. 7 Case 1, ensemble-averaged velocity fields and positions of streamlines near expanding BFS.

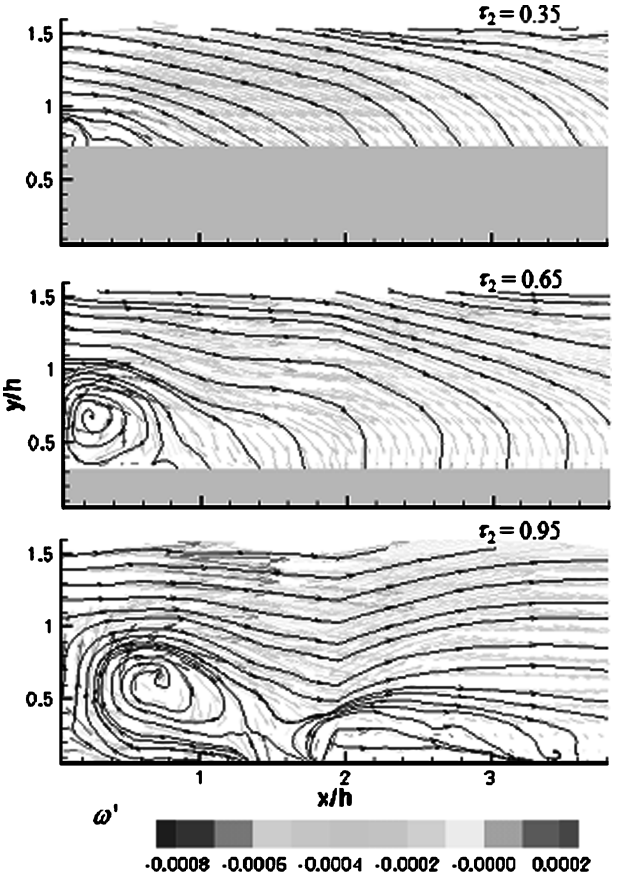

Fig. 8 Case 2, ensemble-averaged velocity fields and positions of streamlines near expanding BFS.

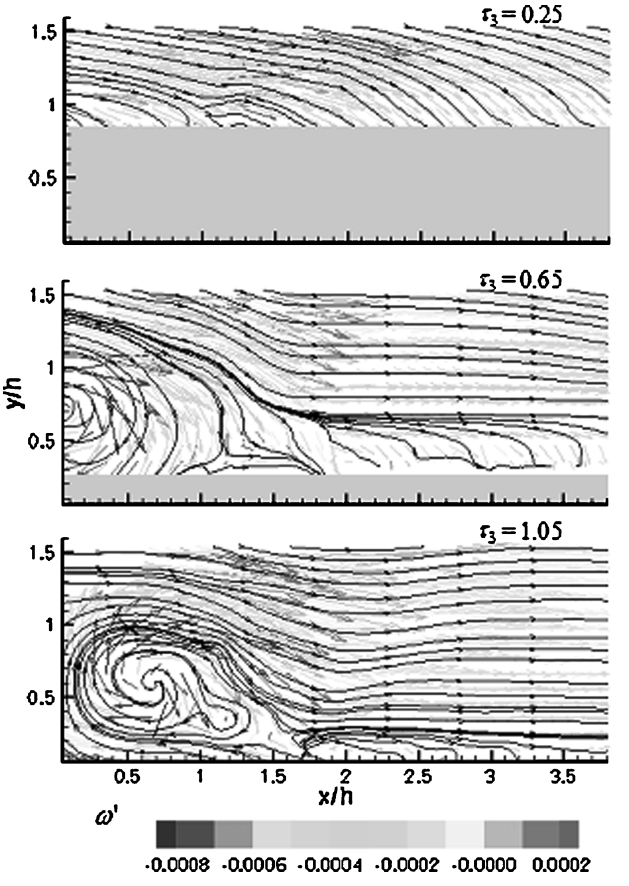

Fig. 9 Case 3, ensemble-averaged velocity fields and positions of streamlines near expanding BFS.

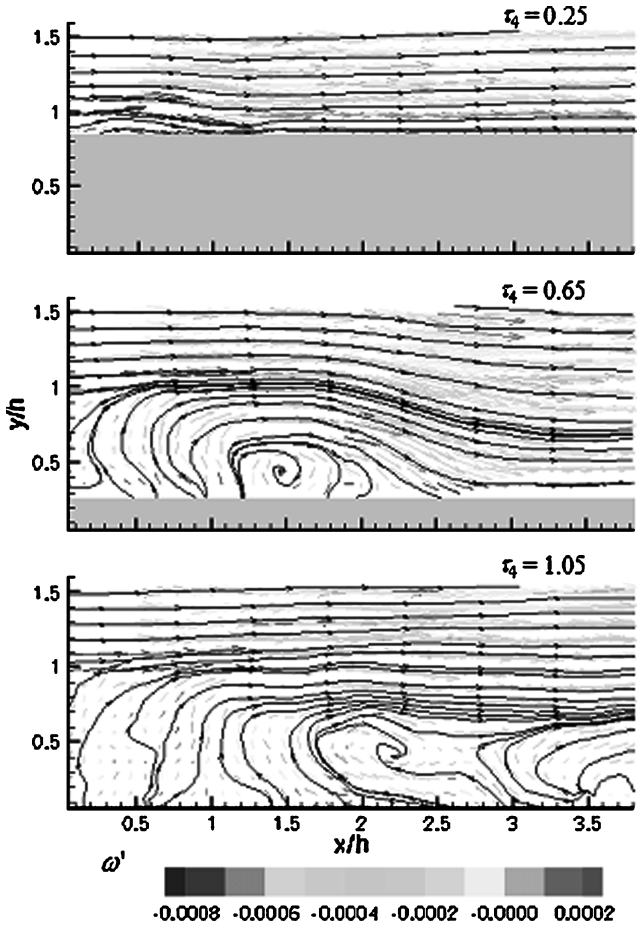

Fig. 10 Case 4, ensemble-averaged velocity fields and positions of streamlines near expanding BFS.

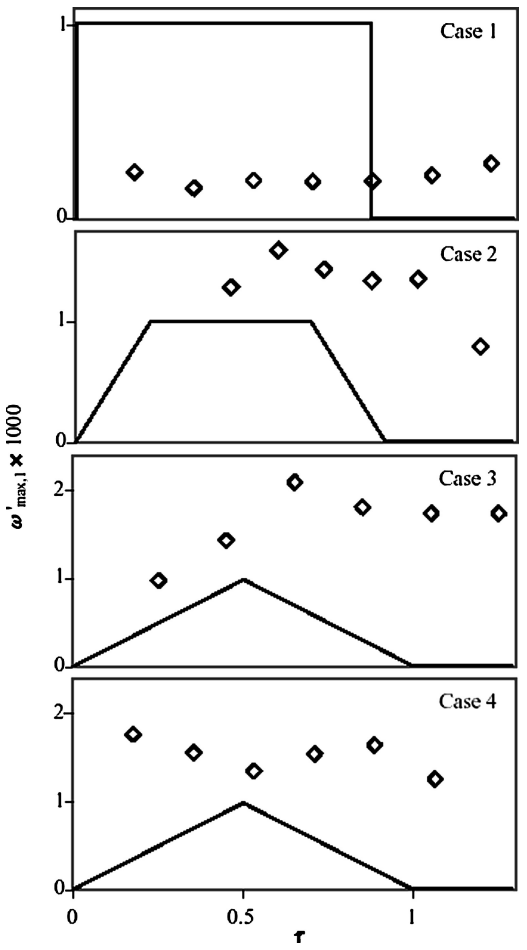

Fig. 11 Normalised value of maximal clockwise vorticity in recirculation zone core for cases 1-4 vs normalised time: ——, normalized velocity of floor.

the BFS; it then moves downstream. The motion of the floor and the presence of a developing recirculation zone cause unsteadiness in the separated shear layer along the surveyed zone (Fig. 8, $\tau_2 = 0.95$). The boundary-layer reattachment region clearly appears for the first time at $\tau = 0.35$ and moves downstream with time.

In case 3 (Fig. 9), the oxidizer flow momentum remains the same as in cases 1 and 2; however, the floor velocity is increased. The flow behavior is similar to that in case 2. In case 4 (Fig. 10), the region of clockwise recirculating flow also appears; however, it is repositioned from the BFS wall to the surface of the floor, at a certain distance (initially 0.5 x/h) from the BFS (Fig. 10, $\tau_4 = 0.25$). The process of recirculation zone enlargement is faster than in cases 2 and 3, and the center of rotation moves downstream and leaves the image area earlier.

Relation Between Oxidizer Flow Momentum and Entrainment Caused by Fuel Regression Simulated by the Floor

The vorticity of the flow, which is a vector measure of the local rotation in the flow, defined mathematically as the curl of the velocity vector, is used for an estimation of the relative importance of the oxidizer flow momentum over the entrainment caused by the fuel regression simulated by the floor. The dependence of the normalized value of the maximal clockwise vorticity $\omega'_{\max}$ in the recirculation zone core on time for cases 1–4 is shown in Fig. 11.

In case 1, the value of the maximal clockwise vorticity ω' is low, and it remains independent of the floor motion, that is, the oxidizer flow momentum dominates over the entrainment caused by the motion of the floor. In case 2, the flow is intensively entrained by the floor, and the floor transfers part of its kinetic energy to the flow. The accelerating motion of the floor causes the normalized maximal clockwise vorticity to increase. Vorticity $\omega'_{\max}$ reaches its maximum before the floor motion deceleration, then it starts to decay. In case 3, the flow behavior is similar to that in case 2. The normalized maximal clockwise vorticity reaches its maximum shortly after the floor deceleration commencement. In case 4, similar to case 1, the maximal clockwise vorticity appears independent of the floor motion.

Generally, the maximal clockwise vorticity in the recirculation zone core is independent of the flow motion in the cases where the oxidizer flow momentum dominates. The value of $\omega'_{\max}$ in the recirculation zone core is proportional to the velocity of the floor. Higher kinetic energy of the floor leads to higher values of the maximal clockwise vorticity.

Discussion

Experiments conducted in LTRAC with a combusting prototype of a high regression rate, liquefying HRM shows a maximal fuel surface regression rate of 0.0011 m/s at an averaged velocity of the oxidizer flow of 28.1 m/s, which makes the ratio U_r of about 25,700. The conditions in this HRM are such that the flow momentum totally dominates and the oxidizer flow probably behaves in a quasi-stationary manner, similar to that demonstrated in case 1 of the current work. Cases 2–4 of low values of U_r correspond to the situations of cases of very high fuel regression rates, something that is very desirable from the point of view of the HRMs thrust output production.

The progressive fuel burn mode is characterized by an accelerating fuel regression rate. Thus, one can expect an increased clockwise vorticity in the zones near the oxidizer port of the HRM and, because of a better mixing of fuel vapors and the oxidizer in this zone, faster consumption of the fuel. Contrary, the regressive fuel burn mode can minimize the clockwise vorticity near the oxidizer port, leading to the formation of a lower fuel regression rate zone that is stretched along the core. However, this conclusion cannot be universal because the vastly different geometrical profiles of the fuel grains may impose additional flow disturbances.

The simulation used here features certain benefits. It enables closer examination of the resulting flow structure and instabilities in the absence of a complex combusting environment. A disadvantage of the isothermal model is that the transfer of kinetic energy between the simulated fuel surface and the oxidizer flow affects the flow behavior. This type of transfer does not occur in combusting HRMs. In addition the proposed simulation is lacking the absence of blowing from the moving floor (as occurring in hybrid rockets and solid-fuel ramjets), which in many cases may significantly affect the flow structure. The existing experimental setup can be improved to provide a better analogy with combusting HRMs, that is, by injecting gas from the surface of the moving section to mimic the production of gaseous products of reaction.

There is an approach in experimental studies and in CFD simulations of SRM used by Dunlap et al.,[14,15] Traineau,[16] and Yamada[17] to treat the burning surface as a porous wall through which mass injection occurs at a given total temperature. However, this approach is limited by the fact that it does not account for the dynamic character of the geometry changes of the core in high regression rate HRMs.

Conclusions

This study shows that the long-time oxidizer flow structure is almost independent of the simulated fuel regression rate. During the regression phase and for cases of high ratio of the oxidizer freestream velocity to the simulated fuel regression rate, the oxidizer flow evolves in a quasi-stationary manner, in which the instantaneous BFS flow structure is akin to that of the static case.

References

[1]Rice, E., St. Clair, C., Chiaverini, M., Knuth, W., Gustafson, R., and Gramer, D., "Initial Test Firing Results for Solid CO/GOX Cryogenic Hybrid Rocket Engine for Mars ISRU Propulsion Applications," *Fifth International Microgravity Combustion Workshop*, NASA Center for AeroSpace Information, Cleveland, OH, May 1999.

[2]Karabeyogly, A., "Transient Combustion in Hybrid Rockets," Ph.D. Dissertation, Stanford Univ., Stanford, CA, Aug. 1998.

[3]Cantwell, B., Karabeyogly, A., and Altman, D., "High Regression Rate Hybrid Rocket Fuels," JIAA TR-122, NASA Ames Research Center, Aug. 1999.

[4]Karabeyoglu, M., Altman, D., and Cantwell, B., "Combustion of Liquefying Hybrid Propellants, Part 1: General Theory," *Journal of Propulsion and Power*, Vol. 18, No. 3, 2002, pp. 610–620.

[5]Karabeyoglu, M., and Cantwell, B., "Combustion of Liquefying Hybrid Propellants, Part 2: Stability of Liquid Films," *Journal of Propulsion and Power*, Vol. 18, No. 3, 2002, pp. 621–630.

[6]Chiaverini, M., Serin, N., Johnson, D., Lu, Y., Kuo, K., and Risha, G., "Regression Rate Behavior of Hybrid Rocket Solid Fuels," *Journal of Propulsion and Power*, Vol. 16, No. 1, 2000, pp. 125–132.

[7]Chiaverini, M., Kuo, K., Peretz, A., and Harting, G., "Regression-Rate and Heat-Transfer Correlations for Hybrid Rocket Combustion," *Journal of Propulsion and Power*, Vol. 17, No. 1, 2001, pp. 99–110.

[8]Stamatov, V., Honnery, D., and Soria, J., "Investigation into the Effects of Expansion Ratio on a Backward Facing Step Flow Using PIV," *7th Asian Symposium on Visualization*, National Univ. of Singapore, Paper 60, Singapore, 2003.

[9]Stamatov, V., Honnery, D., and Soria, J., "PIV Measurements in an Isothermal Model of a High Regression Rate Hybrid Rocket Motor," *5th International Symposium on Particle Image Velocimetry*, Korean Society of Visualization, Paper 14, Busan, Korea, 2003.

[10]Stamatov, V., Honnery, D., and Soria, J., "Effect of Oxidizing Flow Velocity and Burning Rate on Flow Structure in an Isothermal Model of a High Regression Rate Hybrid Rocket Motor," *2003 Australian Symposium on Combustion and the 8th Australian Flames Day*, The Australian Flame Research Committee Inc., Paper 32, Melbourne, Australia, 2003.

[11]Soria, J., "An Investigation of the Near Wake of a Circular Cylinder Using a Video-Based Digital Cross Correlation Particle Image Velocimetry Technique," *Exp Therm Fluid Sci*, Vol. 12, No. 2, 1996, pp. 221–233.

[12]Soria, J., "Multigrid Approach to Cross-Correlation Digital PIV and HPIV Analysis," *13th Australasian Fluid Mechanics Conference*, Vol. 1, edited by M. C. Thompson and K. Hourigan, Melbourne, Australia, 1998, pp. 381–384.

[13]Kostas, J., Soria, J., and Chong, M., "Particle Image Velocimetry Measurements of a Backward-Facing Step Flow," *Experiments in Fluids*, Vol. 33, No. 6, 2002, pp. 838–853.

[14]Dunlap, R., Willoughby, P., and Hermsen, R., "Flowfield in the Combustion Chamber of a Solid Propellant Rocket Motor," *AIAA Journal*, Vol. 12, No. 10, 1974, pp. 1440–1442.

[15]Dunlap, R., Blackner, A., Waugh, R., Brown, R., and Willoughby, P., "Internal Flowfield Studies in a Simulated Cylindrical Port Rocket Chamber," *Journal of Propulsion and Power*, Vol. 6, No. 6, 1990, pp. 690–704.

[16]Traineau, J.-C., Hervat, P., and Kuentzmann, P., "Cold-Flow Simulation of a Two-Dimensional Nozzleless Solid Rocket Motor," AIAA Paper 86-1447, 1986.

[17]Yamada, K., Goto, M., and Ishikawa, N., "Simulative Study on the Erosive Burning of Solid Rocket Motors," *AIAA Journal*, Vol. 14, No. 9, 1976, pp. 1170–1176.